



Modelling and experimental validation of moving tilted volumetric heat source in gas metal arc welding process



Aniruddha Ghosh^a, Anshul Yadav^b, Arvind Kumar^{b,*}

^a Department of Mechanical Engineering, Government College of Engineering & Textile Technology, Berhampore 742101, India

^b Department of Mechanical Engineering, Indian Institute of Technology Kanpur, Kanpur 208016, India

ARTICLE INFO

Article history:

Received 23 March 2016

Received in revised form 7 August 2016

Accepted 8 August 2016

Available online 12 August 2016

Keywords:

Gas metal arc welding

Tilted electrode

Gaussian heat distribution

Ellipsoidal heat source

Heat affected zone

ABSTRACT

In this work, the effect of electrode's tilt angle on transient temperature distribution, heat affected zone width and weld bead geometry in gas metal arc welding process are investigated. Experimental, microstructure and analytical modelling studies of heat affected zone and fusion zone have been performed for different electrode tilt angles. Gaussian heat density distribution and ellipsoidal heat source shape were assumed to predict the transient temperature distribution in the welded plate. The analytical model for the transient temperature distribution in the welded plate considers heat transfers from molten droplets of the filler material, moving volumetric heat source, and convective and radiative heat losses from the welded plate. Decent agreement between the predicted and the experimental temperature distribution, heat affected zone and weld bead geometry is obtained. The comparison suggested that ellipsoidal heat source shape is quite appropriate for predicting the transient temperature distribution on the welded plate for gas metal arc welding process. It was found that the heat affected zone width increases with the decrease in tilt angle. Microstructural examination on samples revealed prominent grain growth in the heat affected zone, however, fine grain structure was observed in the fusion zone. The predictions for heat affected zone width and weld bead geometry are also validated with experiments performed in shop floor welding conditions.

© 2016 Elsevier B.V. All rights reserved.

1. Introduction

Welding is one of the most reliable, efficient and practical metal joining process in existence today. It is widely used in many industries such as nuclear, aerospace, automobile, transportation and off-shore. Heat transfer during the welding process is a complex phenomenon due to the irregular heating and cooling cycles. Due to heating and cooling cycles, complex thermal stresses and strains are produced, resulting in residual stresses, distortions, heat affected zone (HAZ) which has been described in detail in the work by Mahapatra et al. (2006). Consequently, study on heat transfer in welding and transient temperature distribution in weld plate is imperative for controlling the quality of the welded joint. More than seven decades back, Rosenthal (1946) attempted to investigate the transient temperature distribution in the welded plate

considering different heat source shapes (point, line and plane heat source shapes). The concerned model failed to predict transient temperature distribution in the vicinity of welding line with good accuracy due to some unrealistic assumptions. Eager and Tsai (1983) modified the Rosenthal's model and investigated temperature distribution in the weld plate considering 2D surface heat source shape. This model was an important step towards improvement of temperature prediction near the welding line. Nevertheless, this model failed to predict transient temperature distribution along the welding direction accurately. Goldak et al. (1984) initiated consideration of 3D heat source shapes. Since then, significant amount of research work on thermal transport in welding is in progress. Nguyen et al. (1999) developed an analytical model with 3D heat source shape. Double-ellipsoidal heat density moving heat source, semi-infinite body, and conduction heat transfer were in their consideration. They obtained decent agreement between the predicted transient temperatures and the measured ones at various points in bead-on-plate specimens.

Recently, a number of analytical models involving thermal transport phenomena in welding have been developed. An analytical model in rectangular prismatic steel casts regenerated by multi-pass weave bead building up was reported by Winczek

Abbreviations: FSW, friction stir welding; FZ, fusion zone; GMAW, gas metal arc welding; GTAW, gas tungsten arc welding; HAZ, heat affected zone.

* Corresponding author.

E-mail addresses: agmec74@gmail.com (A. Ghosh), anshuly@iitk.ac.in (A. Yadav), arvindkr@iitk.ac.in (A. Kumar).

Nomenclature

A'	Surface area (m^2)
a, b, c	Heat source parameters
c_p	Specific heat metal (electrode and welded plate) ($\text{J kg}^{-1} \text{K}^{-1}$)
h	Convective heat transfer coefficient ($\text{W m}^{-2} \text{K}^{-1}$)
I	Current (A)
k	Thermal conductivity ($\text{W m}^{-1} \text{K}^{-1}$)
L_a	Latent heat of fusion per mass (J kg^{-1})
Δl	Distance travelled by the electrode (m)
M	Maximum heat density (W m^{-3})
Q_0	Rate of volumetric heat generation (m^{-3})
Q_v	Total amount of delivered heat from the molten electrode (W)
q_m	Volumetric heat density of molten weld pool (W m^{-3})
Δq_{ms}	Heat required per unit volume to increase the temperature of the electrode from atmospheric temperature to the melting point temperature (J kg^{-1})
Δq_{hf}	Latent heat of fusion of the electrode material per unit volume (J kg^{-1})
Δq_{ml}	Heat required per unit volume to increase temperature of the electrode from its melting point temperature to the temperature in which droplets of the liquid electrode fall on the surface of the welded plate (J kg^{-1})
T	Temperature ($^\circ\text{C}$)
T^{le}	Temperature of the liquid electrode ($^\circ\text{C}$)
t	Time (s)
T_0	Ambient temperature ($^\circ\text{C}$)
T_m	Melting point temperature (K)
ΔT_1	Temperature field due to heat energy from electric arc ($^\circ\text{C}$)
ΔT_2	Temperature field caused by the convective and radiative heat transfer from the surface ($^\circ\text{C}$)
ΔT_3	Temperature field caused by the deposition of molten electrode ($^\circ\text{C}$)
V	Voltage (V)
v	Travel speed (m s^{-1})
x, y, z	Coordinates (m)
x', y', z'	Coordinates in rotated axis (m)
<i>Greek symbols</i>	
σ	Stefan-Boltzmann constant (W m K^{-4})
ρ	Density of the workpiece (kg m^{-3})
ε	Emissivity of the work piece
θ	Angle ($^\circ$)
α	Thermal diffusivity of the work piece ($\text{m}^2 \text{s}^{-1}$)

(2008). Winczek (2010) presented a model of temperature field in a semi-infinite body caused by heat source with changeable direction of motion. Temperature field in a semi-infinite body during surfacing was reported by Winczek (2011). Winczek (2012) presented a computational methodology for elasto-plastic states for rods subjected to thermal loads. Goyal et al. (2009) presented an analytical model on thermal behaviour and geometry of the weld pool in pulsed current gas metal arc welding (GMAW). They considered two types of heat sources. One was from the droplets of filler metal which were being deposited in the weld pool, and the other was arc heat source. Mishra et al. (2008) reported experimental and modelling results on arc butt welding of stainless steel plates. They studied the effects of welding variables on the weld

pool penetration and width. Bonifaz and Richards (2009) analyzed the transient heat flow and described the solidification structures around the weld pool through a 3D finite element model.

In almost all works, position of the electrode has been considered perpendicular to the surface of the welded plate. However, this may not be the case always. Tilted electrode can have significant influence on transient temperature distribution in the welded plate and other yield parameters of the welding process. It may be noted that only few works have been reported in the area of tilted electrode, however, these were not for the GMAW process. Parvez et al. (2013) developed a 3D model for the gas tungsten arc welding (GTAW) process in order to study the effect of tilt angle on weld pool properties. They observed that for the 90° torch angle, both the arc and weld pool are symmetric, however, for the 70° torch angle these are non-symmetric. Tilting the torch from 90° to 70° increases the temperature distribution on the anode surface ahead of the electrode tip. They reported that for 70° torch angle the weld pool becomes shallow and wide ahead of the electrode tip in the welding direction. Grujicic et al. (2012) reported the effects of weld pitch, tool tilt-angle and tool pin size on the material flow during the friction stir welding (FSW) process using coupled Eulerian and Lagrangian computational analysis. Their results report that highest extent of marker-material mixing/dispersion was attained for 2.5° tool tilt angle. Nilsson et al. (2011) reported implementation of a 3D numerical solver for electric arc welding with tilted electrode motion. Chandel and Hang (1996) studied the effect of current, vertex angle and tilt angle on the plate melting efficiency of an autogenous GTAW process. Klimpel et al. (2006) reported the effect tilt angle on the heat transfer in the plate of gas metal arc surfacing. Kumar and Debroy (2007) discussed heat transfer and fluid flow during gas metal arc fillet welding for tilted moving heat source. They observed that with the increase in tilt angle from -30° to 45°, the horizontal length and the throat of the weld bead decrease while the vertical leg length increases. Parkitny and Winczek (2013) presented an analytical solution of thermal field in semi-infinite body caused by tilted moving heat source. They assumed volumetric heat source with Gaussian heat density distribution. They observed that the weld bead penetration decreases if the electrode is not perpendicular with respect to the welded plate. They also found that if the tilt is opposite to the sense of velocity vector of the heat source, maximum temperature values are much higher than in the case of perpendicular tilt and the head of isotherms is shifted towards the motion of heat source.

GMAW has become a frequently used industrial welding process nowadays. Critical set of input parameters, i.e., current, arc voltage, travel speed, stick out etc., are involved in GMAW process. Engineers often face problems to set appropriate combination of input parameters in order to obtain the desired weld quality. One of the most important issues of GMAW process is HAZ softening that imparts some uncertainties in the weld quality. A significant amount of research work on HAZ width can be found in literature. Parvez et al. (2013) emphasized on the fact that the tilt angle has significant effect on arc temperature, arc velocity, current density, heat flux, electromagnetic force, weld pool, weld bead shape, penetration, bead width. Adequate experimentation to recognize the characteristics of HAZ width under different tilt angles is essential. At the same time, a method to predict the HAZ width is also necessary.

In this work, an analytical model for transient temperature distribution of welded plate has been presented and the HAZ width and weld bead geometry is calculated using this model. In the model, heat transfers from moving volumetric heat source, molten droplet of the filler material, and convective and radiative heat losses from the welded plate are considered. Experimental and microstructural studies of fusion zone (FZ) and HAZ are also performed for different electrode tilt angles. The prediction of HAZ

Table 1

Chemical composition of mild steel workpiece (in weight%).

C	Mn	P	S	Cu	Si	Fe
0.26	1.03	0.04	0.05	0.20	0.28	98.14

Table 2

Process parameters and material properties.

GMAW setup	Fully automatic
Shielding gas	Argon
Power source	Direct current
V-I characteristics	Constant voltage
Electrode	Mild steel (1.3 mm diameter)
GMAW torch	Air cooled
Polarity	Reverse
Current	145 A
Voltage	24 V
Gas flow	$3.5 \times 10^{-4} \text{ m}^3 \text{ s}^{-1}$
Travel speed	2.1 mm s^{-1}
Ambient temperature	313 K
Material of welded plates and electrode	Mild steel
Electrode to work piece distance	2.1 cm
Electrode to work piece angle/tilt angle	$34^\circ, 30^\circ, 26^\circ$
Density of the base material	7850 kg m^{-3}
Melting point of base material	1684 K
Emissivity of the base material	0.28
Latent heat of fusion of base material	247000 J kg^{-1}
Specific heat of base material	$480 \text{ J kg}^{-1} \text{ K}^{-1}$
Thermal conductivity of base material	$50 \text{ W m}^{-1} \text{ K}^{-1}$

width and weld bead geometry using the current model is validated with both laboratory and shop floor welding conditions.

2. Experiments

Automated GMAW unit was used to perform welding experiments on mild steel plates with size 300 mm (length) \times 120 mm (width) \times 23 mm (thickness) in a butt joint configuration. Infrared thermometer (range: 2482 °C, accuracy: ± 2 °C and response time: 10 ms) was used for temperature measurements in the experiments. The composition of mild steel is given in Table 1. In the present study, current, voltage, travel speed, and electrode diameter were fixed and the only variable is electrode tilt angle. Process parameters and other welding conditions, as mentioned in Table 2 are used for experiments. The base case tilt angle is taken as 34° , which is very similar to the usual tilt angles practiced. Two more experiments, with tilt angle 30° and 26° were also been performed. The temperature on the surface of the work piece is measured at three strategic points, $P_1 (x = 4.2 \text{ cm}, y = 0.8 \text{ cm}, z = 0)$, $P_2 (x = 4.2 \text{ cm}, y = 1.4 \text{ cm}, z = 0)$, $P_3 (x = 4.2 \text{ cm}, y = 2.0 \text{ cm}, z = 0)$ (as shown in Fig. 1). Typically, for each case, three welding experiments were performed with identical conditions. The temperature data to be shown in subsequent section represent average values obtained from three experiments performed under identical conditions to establish repeatability of results. Dino-Lite Digital microscope were used to measure HAZ widths and weld bead geometry with the uncertainty of ± 0.001 mm. The overall HAZ width for a sample is estimated as an average value of the measurements at twenty distinct locations. The Microstructural images were taken from Carl Zeiss Axio Imager microscope.

3. Analytical modelling

Transient heat conduction equation (Eq. (1)) is used to analyze the thermal behaviour of the GMAW process.

$$\frac{\partial}{\partial x} \left(k_x \frac{\partial T}{\partial x} \right) + \frac{\partial}{\partial y} \left(k_y \frac{\partial T}{\partial y} \right) + \frac{\partial}{\partial z} \left(k_z \frac{\partial T}{\partial z} \right) + Q_0 = \rho c_p \frac{\partial T}{\partial t} \quad (1)$$

where k (assuming $k_x = k_y = k_z = k$) is the thermal conductivity, Q_0 is the volumetric heat source (caused by electric arc of electrode during welding), ρ is the density, and c_p is the specific heat of the material. It has been assumed that the electrode and the weld plate are of same material (mild steel). The analytical solution of Eq. (1) would represent the temperature distribution as a function of space co-ordinates ($x-z$) and time t .

Ghosh et al. (2013) studied the transient temperature distribution of welded plate in submerged arc welding process. They considered volumetric heat source, heat transfer from the molten electrode and convective heat losses from the welded plate surface. They suggested that the temperature distribution in the weld plate is the sum of all these effects. Hence, the generalized temperature field can be expressed as

$$T(x, y, z, t) - T_0 = \Delta T_1 + \Delta T_2 - \Delta T_3 \quad (2)$$

where ΔT_1 represents the temperature field due to arc heat, ΔT_2 represents the temperature field due to heat transfer from the deposition of molten electrode, and ΔT_3 denotes the temperature field due to the convective and radiative heat transfer from the surface. T_0 is the ambient temperature and the preheating of the plate is zero.

It may be noted that Ghosh et al. (2013) did not consider the radiative heat losses in the term ΔT_3 . Further, the solution presented by them is for a vertical electrode. In this work, an analytical solution for temperature distribution in the welded plate is developed for tilted electrode in GMAW process following a similar methodology as reported in Ghosh et al. (2013). The calculation procedure is presented in subsequent sections.

3.1. Initial and boundary conditions

The specified initial temperature on the entire plate surface is ambient temperature T_0 (313 K). During the welding process, heat is dissipated into the ambient through convection and radiation heat losses from the top surface of the welded plate. Convection and radiation heat losses are also considered on the bottom surface. The heat loss due to convection and radiation over these surfaces is given by

$$-k(T) \frac{\partial T}{\partial n} = h(T - T_0) + \varepsilon \sigma (T^4 - T_0^4) \quad (3)$$

Only convective heat transfer is considered on the lateral surface of the work piece, i.e.

$$-k(T) \frac{\partial T}{\partial n} = h(T - T_0) \quad (4)$$

It may be noted that Eqs. (3) and (4) act as the boundary conditions for Eq. (1).

3.2. Temperature field from the electric arc

The distribution of heat flux from the electric arc is considered as Gaussian distribution with ellipsoidal shape. The 3D ellipsoidal heat source can be considered as superposition of a series of instant point heat sources as suggested by Nguyen et al. (1999). The coordinate system is considered as fixed and Cartesian type. Fig. 2 shows the coordinate system considered after rotation of the axes. It is a mapping from cartesian ($x-z$) coordinate system to another ($x'-z'$) cartesian coordinate system in which the origin is kept fixed and the x' and z' axes are obtained by rotating the x and z axis in counter clockwise direction by an angle θ . The electrode with a tilt angle θ moves along the x axis as shown in Fig. 3 during the welding process. Position of the electrode is tilted with respect to z axis with the angle θ (as shown in Fig. 3).

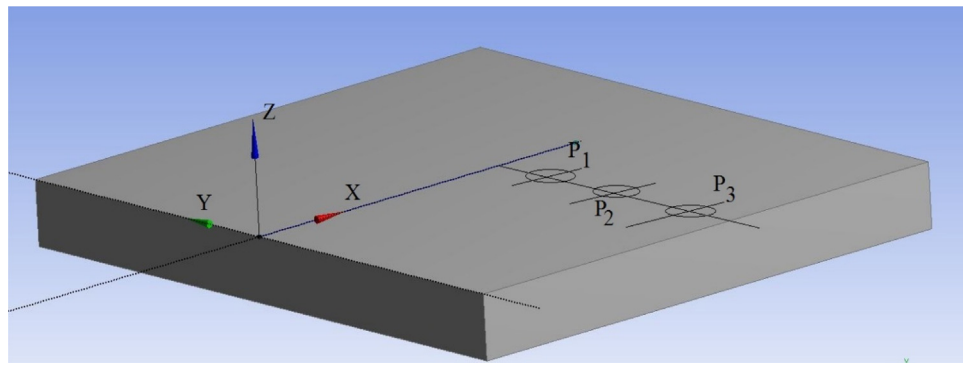


Fig. 1. Schematic diagram of the welded plates, representation of Cartesian coordinate system and location of temperature measurement points P₁ (4.2 cm, 0.8 cm, 0), P₂ (4.2 cm, 1.4 cm, 0), P₃ (4.2 cm, 2.0 cm, 0).

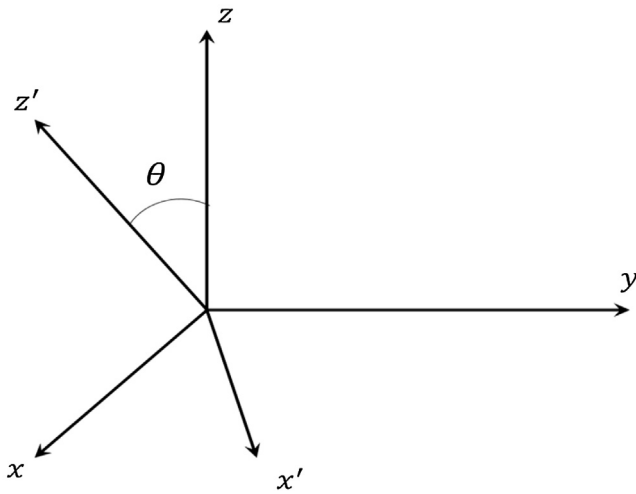


Fig. 2. Coordinate system considered.

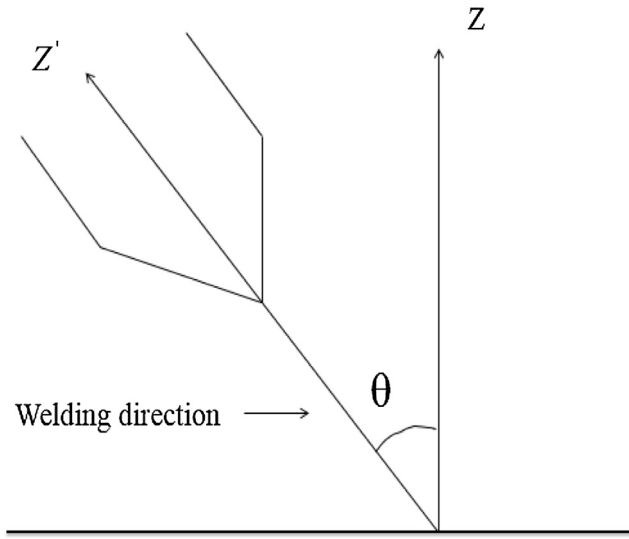


Fig. 3. Representation of tilted electrode.

Let the equation for 3D ellipsoidal heat source shape at a point (x'-z') is

$$q(x', y', z') = M \left(e^{-[a(x')^2 + b(y')^2 + c(z')^2]} \right) \quad (5)$$

where M is the maximum heat density, and $a-c$ are the heat source parameters. $a-c$ are calculated using a similar way as described by [Ghosh and Chattopadhyay \(2013\)](#).

From [Fig. 3](#), $x' = x \cos \theta + z \sin \theta$, $y' = y$ and $z' = z \cos \theta - x \sin \theta$. Thus, Eq. (5) can be written as

$$q(x', y', z') = M \left(e^{-[Ax^2 + By^2 + Cz^2 + Dxz]} \right) \quad (6)$$

where, $A = a \cos^2 \theta + b \sin^2 \theta$, $B = b$, $C = c \cos^2 \theta + b \sin^2 \theta$, $D = (a - c) \sin 2\theta$.

The weld plate has been assumed as semi-infinite body. Hence, the total heat input ($Q_0 = V \times I$) is expressed as

$$Q_0 = M \int_{-\infty}^{\infty} \int_{-\infty}^{\infty} \int_{-\infty}^{0} q(x, y, z) dx dy dz \quad (7a)$$

$$Q_0 = \frac{M}{2} \int_{-\infty}^{\infty} \int_{-\infty}^{\infty} \int_{-\infty}^{\infty} q(x, y, z) dx dy dz \quad (7b)$$

$$2Q_0 = M \int_{-\infty}^{\infty} \int_{-\infty}^{\infty} \int_{-\infty}^{\infty} q(x, y, z) dx dy dz \quad (7c)$$

$$M = \frac{2Q_0 \sqrt{ABC - \frac{BD^2}{4}}}{\pi^{\frac{3}{2}}} \quad (8)$$

Eq. (8) is calculated with the help of Eqs. (A1)–(A5), as described in [Appendix I](#).

In the fixed coordinate system ([Fig. 2](#)) the rise in temperature at a point (x''-z'') at time t'' with dQ amount of heat placed for a small interval of time dt'' is given as

$$dT = \frac{dQdt''}{\rho c_p [4\pi\alpha(t - t'')]^{\frac{3}{2}}} e^{-\left[\frac{(x-x'')^2 + (y-y'')^2 + (z-z'')^2}{4\pi\alpha(t-t'')} \right]} \quad (9)$$

where α is the thermal diffusivity of the material. Hence, the transient temperature distribution due to heat transfer from the electric arc of electrode can be obtained by integrating Eq. (9) as

$$dT_1 = \frac{1}{2} \int_{-\infty}^{\infty} \int_{-\infty}^{\infty} \int_{-\infty}^{\infty} \frac{q(x'', y'', z'') dx'' dy'' dz'' dt''}{\rho c_p [4\pi\alpha(t - t'')]^{\frac{3}{2}}} e^{-\left[\frac{(x-x'')^2 + (y-y'')^2 + (z-z'')^2}{4\pi\alpha(t-t'')} \right]} \quad (10)$$

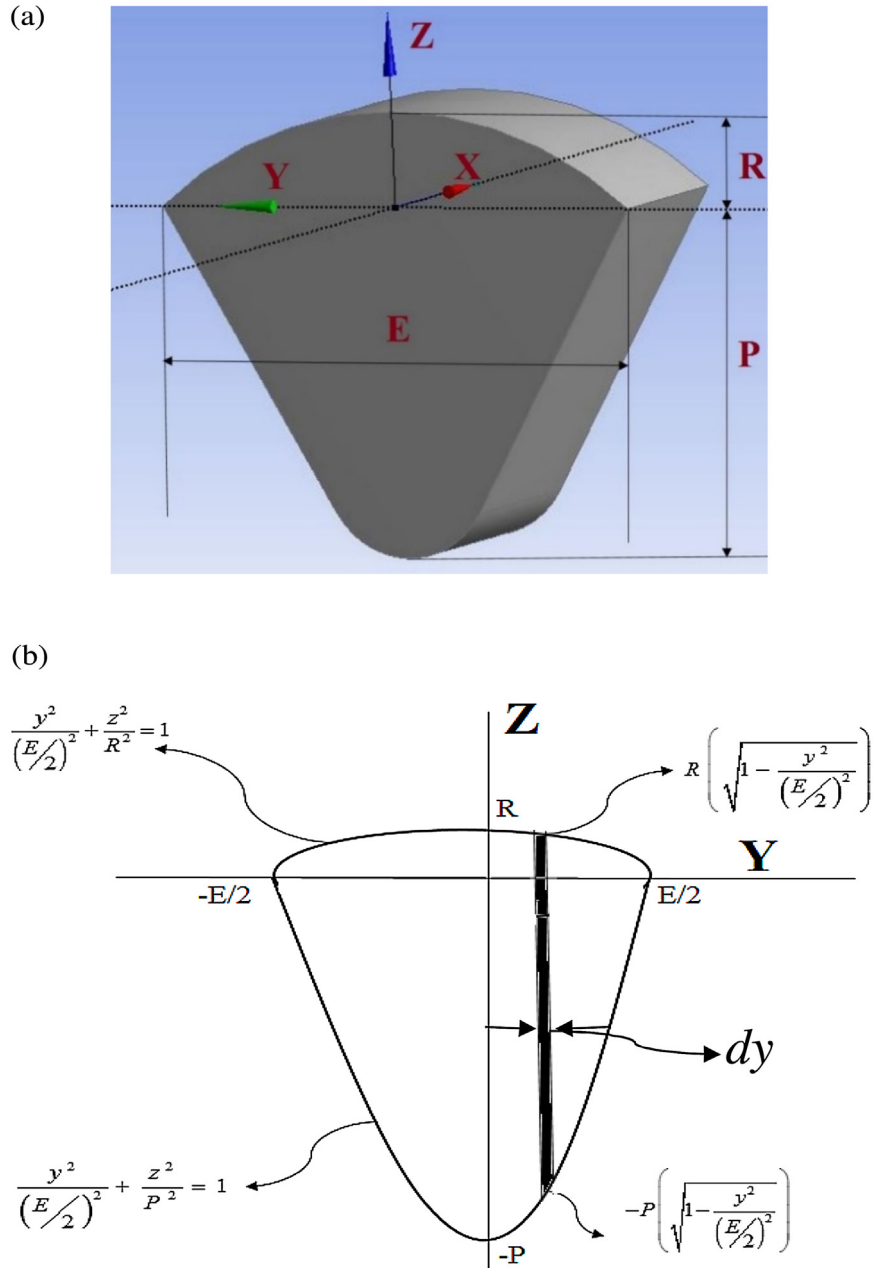


Fig. 4. (a) Schematic view of weld pool (b) 2D view of weld pool. R – Reinforcement height, P – Penetration, E – Bead. Equations of the upper semi-ellipsoid and the lower semi-ellipsoid are $\frac{y^2}{(\frac{E}{2})^2} + \frac{z^2}{R^2} = 1$ and $\frac{y^2}{(\frac{E}{2})^2} + \frac{z^2}{P^2} = 1$, respectively.

When heat source is moving with constant speed v from time $t'' = 0$ to $t'' = t$, the increase in temperature during this time is given as

$$\Delta T_1 = \int_0^t \frac{\sqrt{\pi}}{\sqrt{j}} \times e^{-i t^2 j} \times \frac{\sqrt{\pi}}{\sqrt{m}} \times e^{-\left(o_t - \frac{n_t^2}{m}\right)} \frac{\sqrt{\pi}}{\sqrt{p}} e^{-w} dt'' \quad (11)$$

Eq. (11) is derived with the help of Eqs. (A6)–(A20), as described in Appendix II. Eq. (11) describes the calculation of the first term, ΔT_1 , in the temperature field Eq. (2).

3.3. Temperature field due to molten electrode material

Fig. 4 (a) and (b) show schematic diagrams of the weld bead geometry and 2D view of the weld pool, respectively. Heat transfer from molten electrode is one of the causes of transient temperature change of the welded plate. In this perspective, a combination of two semi-ellipsoidal shapes of weld pool (one is above the y axis and other is below the y axis), as shown in Fig. 4(b), is considered. The lower and upper limits of integration of z coordinate for the weld pool is expressed as $z = -P$ and $z = R$, where P is the penetration depth and R is the reinforcement height.

The total amount of heat transported from the molten electrode is expressed as

$$Q_v = \int_0^{\Delta l} \left(\int_{-\frac{E}{2}}^{\frac{E}{2}} \left(\int_{-P}^{R \sqrt{1 - \frac{y^2}{(\frac{E}{2})^2}}} q_m dz \right) dy \right) dx \quad (12)$$

where, q_m is the heat density of the molten electrode and Δl is the distance travelled by the electrode in one second.

The heat density of molten electrode is considered as in Ghosh et al. (2013)

$$q_m = (\Delta q_{ms} + \Delta q_{hf} + \Delta q_{ml}) \quad (13)$$

where Δq_{ms} is the heat energy required per unit volume to increase the temperature of the electrode from atmospheric temperature to melting point temperature, Δq_{hf} is the latent heat of fusion of the electrode material per unit volume, and Δq_{ml} is the heat energy required per unit volume to increase the temperature of the electrode from its melting point temperature to the temperature at which droplets of the liquid electrode fall on the surface of the welded plate.

$$\Delta q_{ms} = \rho c_p (T_m - T_0) \quad (14a)$$

$$\Delta q_{hf} = \rho I_a \quad (14b)$$

$$\Delta q_{ml} = \rho c_p (T^{le} - T_m) \quad (14c)$$

where T_m is the melting point temperature of the electrode, T_0 is the ambient temperature and T^{le} is the temperature of the molten droplet which is measured during the welding experiment.

For the heat q_m applied at a point $(x-z)$, the elementary temperature rise is expressed as

$$dT_2 = \frac{q_m dx'' dy'' dz''}{\rho c_p [4\pi\alpha(t-t'')]^{3/2}} e^{-\left[\frac{(x-x'')^2+(y-y'')^2+(z-z'')^2}{4\pi\alpha(t-t'')}\right]} \quad (15)$$

Therefore, the temperature increase due to heat transfer from molten electrode for time t is expressed as

$$\Delta T_2 = \int_0^t \left(\int_0^{\frac{\Delta l}{2}} \left(\int_{-\frac{E}{2}}^{\frac{E}{2}} \left(\int_{-P}^{R \sqrt{1 - \frac{y^2}{(\frac{E}{2})^2}}} \frac{q_m}{\rho c_p [(4\pi\alpha(t-t'')]^{3/2}]^{3/2}} \times e^{-\left[\frac{(x-x'')^2}{4\alpha(t-t'')} + \frac{(y-y'')^2}{4\alpha(t-t'')} + \frac{(z-z'')^2}{4\alpha(t-t'')} + \frac{(y-y'')^2}{4\alpha(t-t'')} + \frac{(z-z'')^2}{4\alpha(t-t'')} + \frac{(z-z'')^2}{4\alpha(t-t'')} dz''\right]} dy'' \right) dx'' \right) dt'' \right) \quad (16)$$

Eq. (16) is derived with the help of Eqs. (A21)–(A23), as described in Appendix III. Eq. (16) describes the calculation of the second term, ΔT_2 , in the temperature field Eq. (2).

3.4. Temperature drop due to convective and radiative heat transfer

Let the temperature drop due to convective and radiative heat losses from the surface of the welded plate in the differential time interval of dt'' is dT . Therefore, energy balance from the weld plate in that time interval is

$$[h_c A'(T - T_0)]dt'' = \rho c_p \bar{V} dt'' \quad (17)$$

where, \bar{V} is the volume, A' is the surface area of the work piece, and h_c is the combined heat transfer coefficient when radiative and convective heat transfer are involved in a process. According to Goldak and Akhlaghi (2006), h_c can be defined as $h_c = 24.1 \times 10^{-4} \varepsilon T^{1.61}$

When the heat source is moving with constant speed v from time $t'' = 0$ to $t'' = t$, the change in temperature for a specified position on welded plate during this time can be calculated as

$$\int_0^t dt'' = \int_{T_0}^T \frac{\rho c_p \bar{V} dT}{24.1 \times 10^{-4} \varepsilon T^{1.61} (T - T_0)} \quad (18a)$$

$$\int_0^t dt'' = \int_{T_0}^T \frac{\rho c_p \bar{V} dT}{24.1 \times 10^{-4} \varepsilon T^{2.61} (1 - \frac{T_0}{T})} \quad (18b)$$

$$\int_0^t dt'' = \int_{T_0}^T \frac{T^{-2.61} \times (1 - \frac{T_0}{T})^{-1} \rho c_p \bar{V} dT}{24.1 \times 10^{-4} \varepsilon} \quad (18c)$$

Since, T is much greater than the value of T_0 , Eq. (18c) can be written using power series expansion as

$$\int_0^t dt'' = \int_{T_0}^T \frac{T^{-2.61} \times (1 + \frac{T_0}{T}) \rho c_p \bar{V} dT}{24.1 \times 10^{-4} \varepsilon} \quad (19a)$$

$$\int_0^t dt'' = \int_{T_0}^T \frac{\rho c_p \bar{V}}{24.1 \times 10^{-4} \varepsilon} \times (T^{-2.61} + T^{-1.61} T_0) dT \quad (19b)$$

$$t = \frac{\rho c_p \bar{V}}{24.1 \times 10^{-4} \varepsilon} \times \left[\frac{T^{-1.61}}{-1.61} - \frac{T_0^{-1.61}}{-1.61} + \frac{T_0 T^{-0.61}}{-0.61} - \frac{T_0^{0.39}}{-0.61} \right] \quad (19c)$$

$$t = \frac{\rho c_p \bar{V}}{24.1 \times 10^{-4} \varepsilon} \times \left[\frac{T_0^{-1.61}}{1.61} + \frac{T_0^{0.39}}{0.61} - \left(\frac{(\Delta T_3 + T_0)^{-1.61}}{1.61} + \frac{T_0(\Delta T_3 + T_0)^{-0.61}}{0.61} \right) \right] \quad (19d)$$

where $\Delta T_3 = T - T_0$. Equation (19d) describes the calculation of the third term, ΔT_3 , in the temperature field Eq. (2).

With the calculation of $\Delta T_1 - \Delta T_3$, as described in the previous sections, the temperature field given by Eq. (2) can be predicted.

4. Results and discussion

4.1. Transient temperature distribution

The base case tilt angle is taken as 34° which is very similar to the usual tilt angles practiced. Two more experiments with tilt angle 30° and 26° have also been performed in order to study the effects of tilt angle on weld characteristics. As already mentioned, the temperature on the surface of the work piece is measured at strategic points P_1 (4.2 cm, 0.8 cm, 0.0), P_2 (4.2 cm, 1.4 cm, 0.0), P_3 (4.2 cm, 2.0 cm, 0.0). Fig. 5 shows the measured transient temperature distribution on the welded plate for different electrode tilt angles. The temperature predicted from the analytical method and that obtained from the experimental measurements are compared in Figs. 6–8 for the base case of 34° tilt angle. In the present analytical solution, latent heat of fusion, convective and radiative heat loss have been considered but variable thermo-physical properties

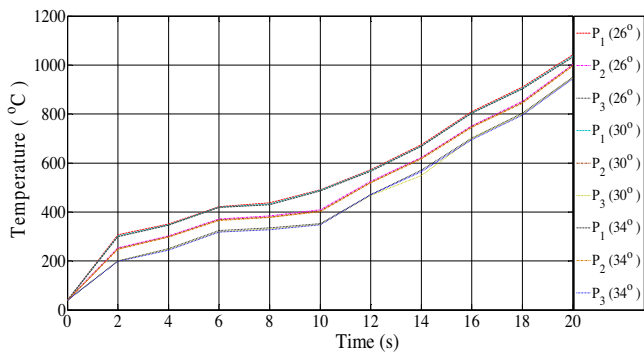


Fig. 5. Measured transient temperature distribution on the welded plate for different tilt angles of the electrode (34°, 30°, 26°).

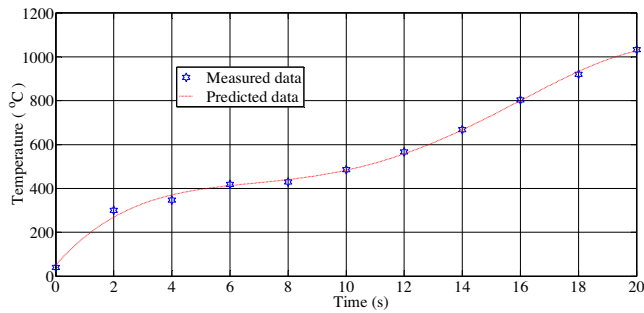


Fig. 6. Comparison of the predicted and measured transient temperature profile at the location P₁ for 34° tilt angle.

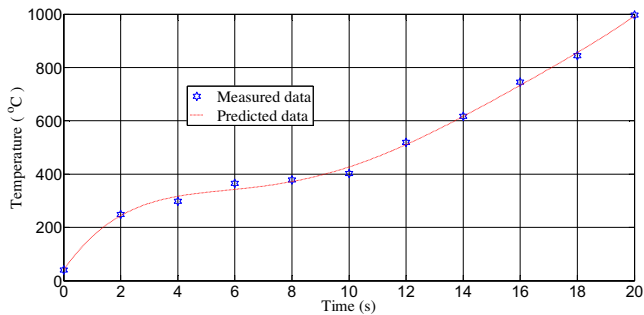


Fig. 7. Comparison of the predicted and measured transient temperature profile at the location P₂ for 34° tilt angle.

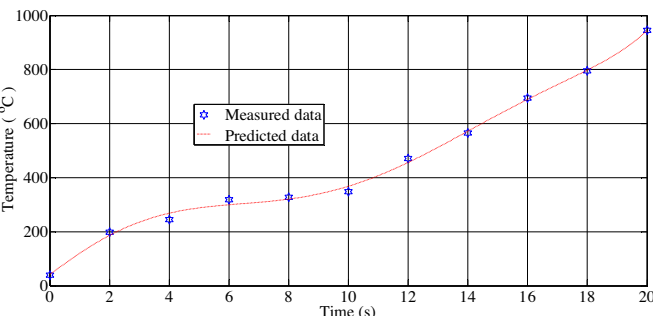


Fig. 8. Comparison of the predicted and measured transient temperature profile at the location P₃ for 34° tilt angle.

have not been included. Therefore, near the welding line, the error is about 7%. However, for locations away from the welding line the comparison is fairly decent with variation of less than 3%. It can be comprehended from Fig. 6 that the measured temperature at the

Table 3
Comparison of predicted and measured HAZ width.

Tilt angle of electrode	Measured HAZ width (mm) (measurement uncertainty is ± 0.001 mm)	Predicted HAZ width (mm)	% difference
34°	1.630	1.773	8.06
30°	1.798	1.971	8.78
26°	1.854	2.016	8.04

location P₁ (4.2, 0.8, 0) at time $t = 4$ s is 346 °C, whereas the predicted temperature is 373 °C. At time $t = 18$ s, the measured temperature is 909 °C, whereas the predicted temperature is 945 °C. From Fig. 7 it can be seen that the measured temperature at the location P₂ (4.2, 1.4, 0) at time $t = 4$ s is 298 °C, whereas the predicted temperature is 306 °C. At time $t = 18$ s, the measured temperature is 844 °C, whereas the predicted temperature is 867 °C. Similarly, from Fig. 8 it can be seen that measured temperature at the location P₃ (4.2, 2, 0) at time $t = 4$ s is 245 °C, whereas the predicted temperature is 252 °C. Later at time $t = 18$ s, the measured temperature is 782 °C, whereas the predicted temperature is 798 °C.

It was revealed from the experiments that the temperature on the welded plate is maximum near the weld line and decreases away from the weld line as heat density distribution near the welding line is maximum which is distributed in Gaussian manner. It was also observed that convective and radiative heat loss has major role on the transient temperature distribution of the welded plate. Heat is transferred from FZ to HAZ by conduction during the welding process. When the tilt angle of the electrode is 34°, temperature at the point P₁ (i.e., at location $x = 4.2$ cm, $y = 0.8$ cm, $z = 0.0$), initially was 40 °C. After 2 s from starting of the welding process, the temperature of this point rises to 306 °C, after 18 s it becomes 910 °C and after 20 s the temperature becomes 1041 °C. In aforesaid same time intervals, temperature of points P₂ (i.e., at location $x = 4.2$ cm, $y = 1.4$ cm, $z = 0.0$) and P₃ (i.e., at location $x = 4.2$ cm, $y = 2.0$ cm, $z = 0.0$) are 252 °C, 852 °C, 1001 °C; and 40 °C, 201 °C, 803 °C, 951 °C, respectively. As can be seen in Fig. 1, P₁–P₃ locations are such that P₃ is the farthest from the centre and P₁ is the closest. If there were no convective and radiative heat losses during welding process, then slope of temperature curves in Fig. 5 would be higher. As a result, the value of temperatures would have been more with respect to the data shown in Fig. 5. However, the experimental results show that the curve is not so steep, which suggests that convective and radiative heat losses were present. It may be noted that the present analytical model considers these effects. It was also observed that as the tilt angle decreases, the temperature away from the electrode becomes lower as the minor axis of ellipsoidal heat source increases.

4.2. Heat affected zone

The region in the welded material, where peak temperature is below the melting temperature while high enough that the microstructure of the material in that region changes is called HAZ. The change in microstructure in HAZ depends on the input parameters, such as amount of heat input, peak temperature reached, rate of cooling and tilt angle of electrodes. This zone is the weakest section in a welded plate. Although the effect of welding parameters on HAZ width has been studied, very little attention was paid to the effect of electrode tilt angle. In this study, HAZ width and weld bead geometry are predicted with the help of Eqs. (2), (11), (16) and (19d) as expressed in Appendix IV. The experimental HAZ widths are tabulated in Table 3. The overall HAZ width for a sample is estimated as an average value of the measurements at twenty distinct locations. The sample HAZ width in the half of the welded plate for tilt angle of 34° is shown in Fig. 9. The mea-

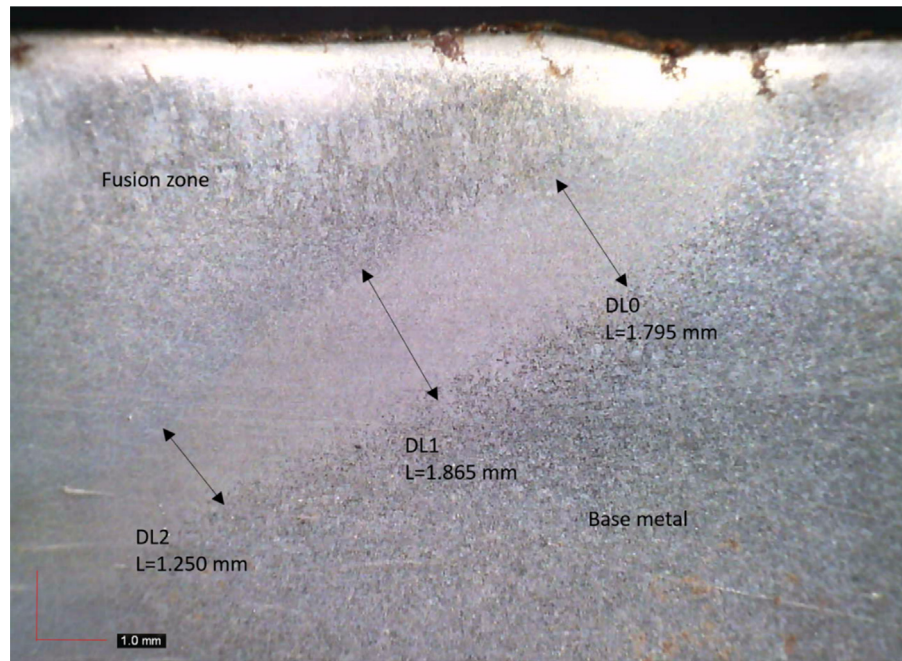


Fig. 9. Measurement of the heat affected zone of the welded plate for 34° tilt angle.

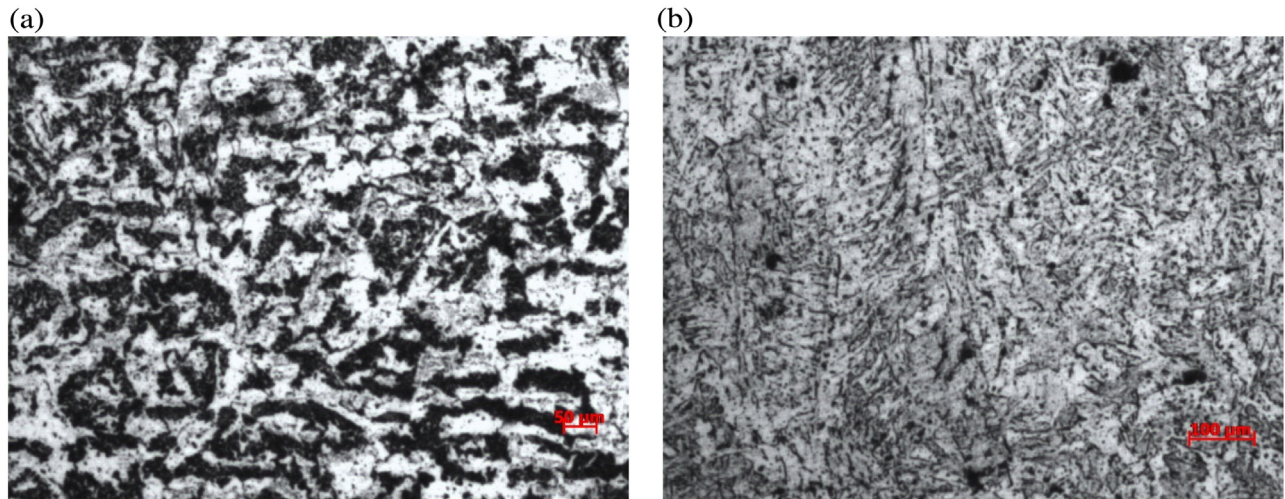


Fig. 10. Microstructure of the welded plate for 34° tilt angle (a) heat affected zone, (b) fusion zone.

Table 4
Comparison of predicted and measured weld bead geometry.

Tilt angle of electrode	Penetration (mm)			Bead width (mm)		
	Measured (measurement uncertainty is ± 0.001 mm)	Predicted	% difference	Measured (measurement uncertainty is ± 0.001 mm)	Predicted	% difference
34°	4.24	4.79	11.48	15.85	17.79	10.91
30°	4.30	4.86	11.52	15.90	17.97	11.52
26°	4.34	4.89	11.25	15.86	17.82	11.00

sured average value is 1.630 mm, whereas the predicted value is 1.773 mm. Fig. 10(a), (b) shows the microstructural views of HAZ and FZ, respectively for 34° tilt angle. HAZ width for 30° tilt angle is 1.798 mm (as shown in Fig. 11), whereas the predicted value is 1.971 mm. Fig. 12(a), (b) shows the microstructural views of HAZ and FZ, respectively for 30° tilt angle. Similarly, HAZ width for 26° tilt angle is 1.854 mm (as shown in Fig. 13), whereas the predicted value is 2.016 mm. Fig. 14(a), (b) shows the microstructural views of

HAZ and FZ, respectively for 26° tilt angle. From Figs. 10(b), 12(b), 14(b) it can be observed that the microstructure in the centre of the weld metal is completely different from other zones because of rapid cooling at this location. For 0° tilt angle the predicted values for HAZ is 2.037 mm. It has been observed from the above discussion that the HAZ width increases with the decrease of tilt angle. Tilt angle influences HAZ width as well as bead geometry. It was revealed from the experimental results as tabulated in Table 4 that

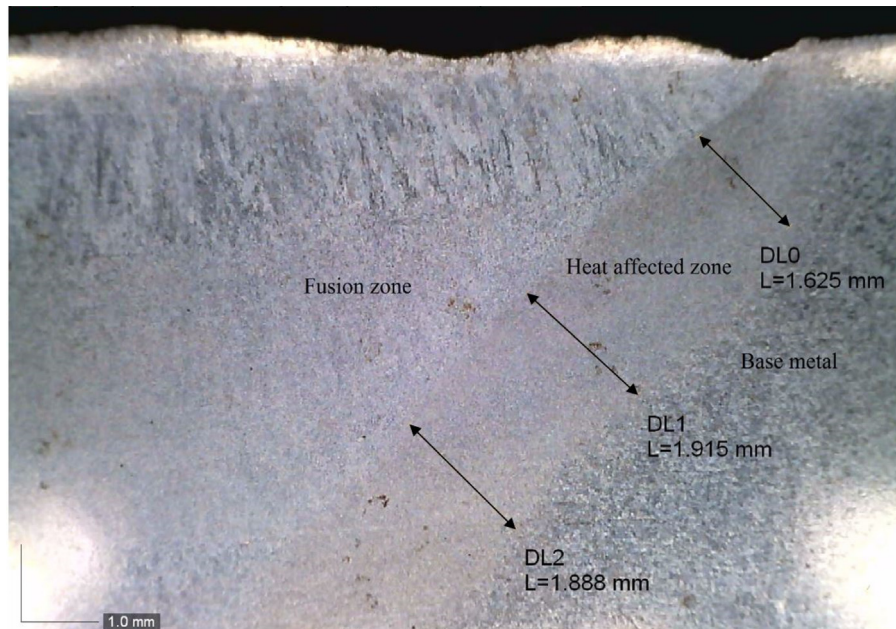


Fig. 11. Measurement of the heat affected zone of the welded plate for 30° tilt angle.

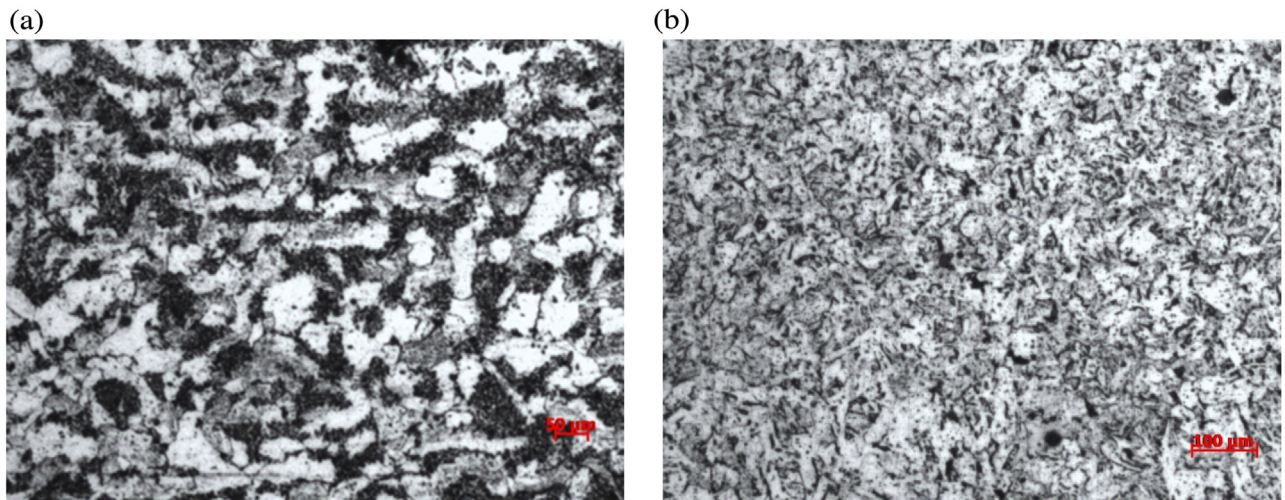


Fig. 12. Microstructure of the welded plate for 30° tilt angle (a) heat affected zone, (b) fusion zone.

when tilt angle of electrode decreases, the peak value of heat density distribution near the weld line increases. Therefore, the minor axis of ellipsoidal heat source along y and z axis is increased but along the major x axis of ellipsoidal heat source decreases. Increase in peak value of the heat density distribution results in larger weld pool along y and z axis, which can also be observed from Table 4. Therefore, for lower tilt angle, a longer minor axis along y and z axes of ellipsoidal heat source results in larger penetration, bead width and HAZ width. Then, due to increase of pick heat density distribution consequent cooling rate decreases. Hence, chance of getting a larger HAZ width becomes higher which can be verified from Table 3.

As shown in Table 3 the predicted HAZ width differs by about 8% from the experimental measurement. The reason for this difference could be the variation of thermophysical properties as a function of temperature, and high temperature near the welding line. In the current analytical solution they were assumed as constant.

There is not much microstructural difference for different tilt angle as revealed from Figs. 10, 12, 14. Prominent grain growth in

HAZ was revealed in Figs. 10(a), 12(a), 14(a) and Fig. 15. This is due to the heat trapped for sufficient time in the HAZ the welded plate with temperature above the lower critical temperature. Figs. 10(b), 12(b) and 14(b) represent microstructure of FZ. Here, fine grain structure is observed.

In Fig. 15 the FZ boundary is distinguishably visible and may be referred to as fusion line. Effect of heat flow can be clearly seen from the microstructure. Heat was flowing from the weld pool to the base metal as shown by green arrow. Therefore, the temperature of the base metal was above the lower critical temperature (1000 K) for a sufficient time. Due to this it results in elongation of ferrite grains in this region. It can also be seen that the grain growth was prominent in this region. Boumerzoug et al. (2010) reported that in HAZ solid state phase transformation takes place and it comprises of clusters of pearlite and ferrite. Hence, prominent grain growth, annealing, phase transitions, recrystallization and tempering occur in the HAZ of mild steel welds. As seen in the HAZ in Fig. 15 clusters of pearlite and ferrite are observed in the HAZ. Larger grains are found in the portion of the HAZ which is near to the FZ. The microstructure in the

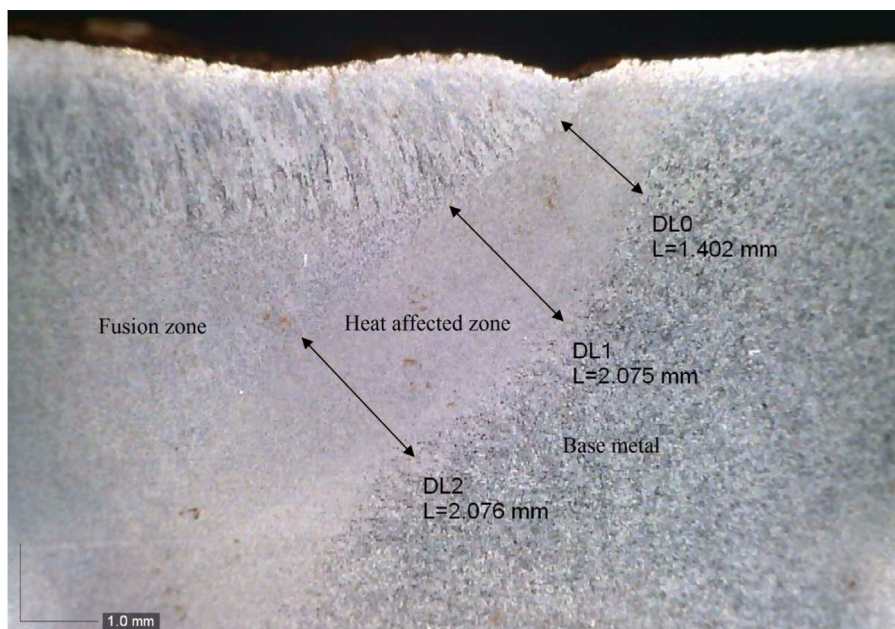


Fig. 13. Measurement of the heat affected zone of the welded plate for 26° tilt angle.

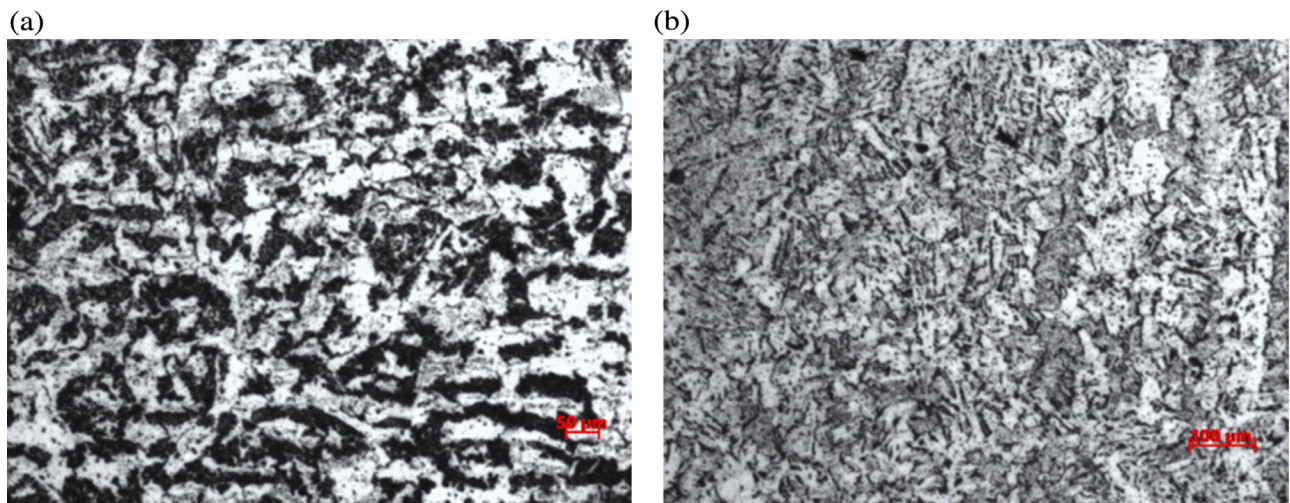


Fig. 14. Microstructure of the welded plate for 26° tilt angle (a) heat affected zone, (b) fusion zone.

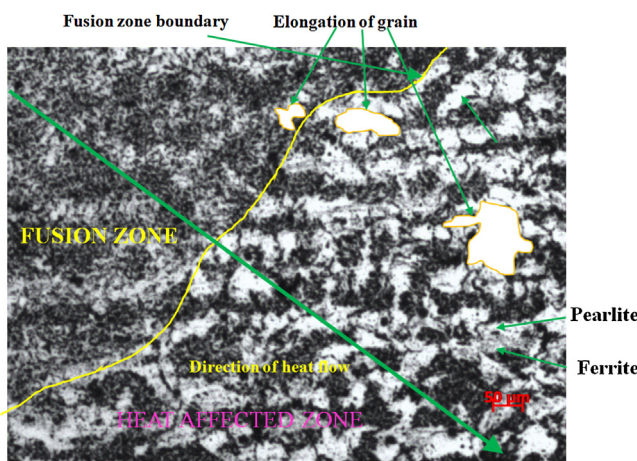


Fig. 15. Distinct microstructure of the fusion zone and the heat affected zone for 34° tilt angle.

weld is heterogeneous due to temperature gradients and chemical gradients that evolve during the process.

4.3. Penetration and bead width

If current increases then metal deposition rate, penetration and reinforcement height also increases but bead width decreases. Hence, it can be understood that for a given tilt angle, the increase in current density leads to increase in the penetration depth. However, for a given current density the change in the tilt angle has an effect on length of the minor axis along y , z direction of the ellipsoidal heat source. Therefore, when the tilt angle decreases then the relative heat density distribution along y and z axis increases and therefore the bead width and penetration increases. Accordingly, the current density and the tilt angle have interacting effect on the weld bead geometry. Table 4 provides details of the predicted and the measured values of penetration and bead width. Procedure of prediction of penetration and weld bead are explained in Appendix IV. It can be seen that the penetration and bead width have inverse

Table 5

Welding conditions used in Moghaddam et al. (2016).

Welding speed (S) (cm/min)	Voltage (V)	Groove angle (degree)	Current (A)
25	40	90	145

effect with tilt angle. The errors in predictions and measurements are near about 11% as shown in Table 4. The penetration and bead width are the characteristics of the FZ in the weld pool along z and y direction, respectively where the peak temperature is high. The thermo-physical property can vary significantly in this zone. The consideration of constant thermo-physical properties in the model may be the reason for errors observed between the predictions and the measurements.

Fig. 16(a) is the representation of the axis system, HAZ width and penetration in bead geometry. Fig. 16(b) shows the experimentally measured values of penetration, bead width and reinforcement height for the base case of tilt angle 34°. These values for all cases of tilt angles are tabulated in Table 4. For 0° tilt angle the predicted values for penetration and bead width are 5.49 mm and 17.43 mm, respectively. It can be clearly interpreted that increase in the tilt angle slightly decreases the penetration, however, the bead width is unaffected.

4.4. Capability of the model in practical welding conditions

In this paper, an analytical method is developed to predict temperature of the weld plate and the weld bead geometry parameters. The model is valid for various range of welding parameters, including typical laboratory as well as actual shop floor welding conditions. Because of simplicity in use, and robustness under various parametric conditions, and no need of a sophisticated computational model, analytical methods can be effectively used to select a first-order estimate of optimal welding parameters. It must be noted that without going into complex computational modelling, temperature and bead geometry can be found with good level of confidence with the help of this model. As shown previously the model is well-validated with the in-house experimental results.

The welding conditions used in the experiments are typical laboratory conditions which are limited by the typical capability of welding equipment. However, it must be noted that the conditions are well controlled in these laboratory experiments. Also, the experiments are repeated in the same welding conditions ensure the repeatability of the results. The model predictions agree well with the laboratory experimental results. After this validation, it is worthwhile to validate the model with actual shop floor conditions as well. In this section, comparison and validation of the predicted results from the current model under shop floor welding conditions is described. Comparison between the predicted bead geometry HAZ width, bead width and penetration is performed from the experimental data of Moghaddam et al. (2016).

The welding conditions are given in Table 5 (Moghaddam et al., 2016). These experiments were performed for 0° tilt angle. Comparison results for penetration and bead width are tabulated in Table 6. The predictions agree well with the experimental results. Table 6 also shows predictions when the tilt angle is changed to 34°. As can be seen, in these actual shop floor welding conditions also the tilt

Table 6

Comparison of predicted penetration and bead width with experimental results of Moghaddam et al. (2016).

S. No.	Tilt angle	Penetration (mm)			Bead width (mm)		
		Prediction	Experimental	% difference	Prediction	Experimental	% difference
1	0	4.67	5.14	9.14	11.46	10.33	10.12
2	34	4.12	-	-	12.72	-	-

Table 7

Comparison of predicted HAZ width with experimental results of Moghaddam et al. (2016).

S. No.	Tilt angle	Heat affected zone width (mm)		
		Prediction	Experimental	% difference
1	0	3.82	4.25	10.12
2	34	2.99	-	-

angle has significant influence on the weld characteristics. Comparison result for HAZ width is shown in Table 7. The predictions compare well with the experimental results. Table 7 also shows predictions for 34° tilt angle. Again it shows that the tilt angle has significant influence.

These results illustrate applicability of the model in shop floor welding condition as well. The first order estimate about the temperature and the bead geometry predictions can be very useful for designing the optimum welding conditions.

5. Conclusions

An analytical model for transient temperature distribution of gas metal arc welded plate for titled electrode has been presented. Experimental and microstructural studies of FZ and HAZ have also been performed for different electrode tilt angles. The prediction of HAZ width and weld bead geometry using the current model is validated with both laboratory and shop floor welding conditions. From this study the following conclusions were drawn:

- Comparison of the measured and the predicted temperature data suggests that consideration of ellipsoid heat source shape for predicting the transient temperature distribution on the welded plate is quite appropriate for GMAW process.
- Temperature away from the welding line along the y axis decreases with increase of tilt angle as minor axis of ellipsoidal heat source decreases with increase in the tilt angle.
- HAZ width increases with decrease in the tilt angle. For lower tilt angles, the increased heat density distribution along the z and y directions results in a large weld pool size along z and y axes. Therefore, a larger minor axis of the ellipsoidal heat source for lower tilt angle results in larger HAZ width.
- The predicted temperature distributions obtained through the analytical method and those obtained from the experimental measurements compared fairly well with variation less than 3% for locations away from the welding line. Near the welding line the difference is about 7%. Error in the predicted HAZ width is about 8%.
- Weld bead dimensions are predicted through the analytical model and its comparison with the experimental measurement shown a difference of about 11%. Increase in the tilt angle slightly increases the bead width, and slightly decreases the penetration.
- Regions near to HAZ show the effect of direction of the heat flow as elongated ferrite grains are observed in these regions.
- The proposed model is able to predict weld bead geometry in actual shop floor welding conditions with a good level of confidence.

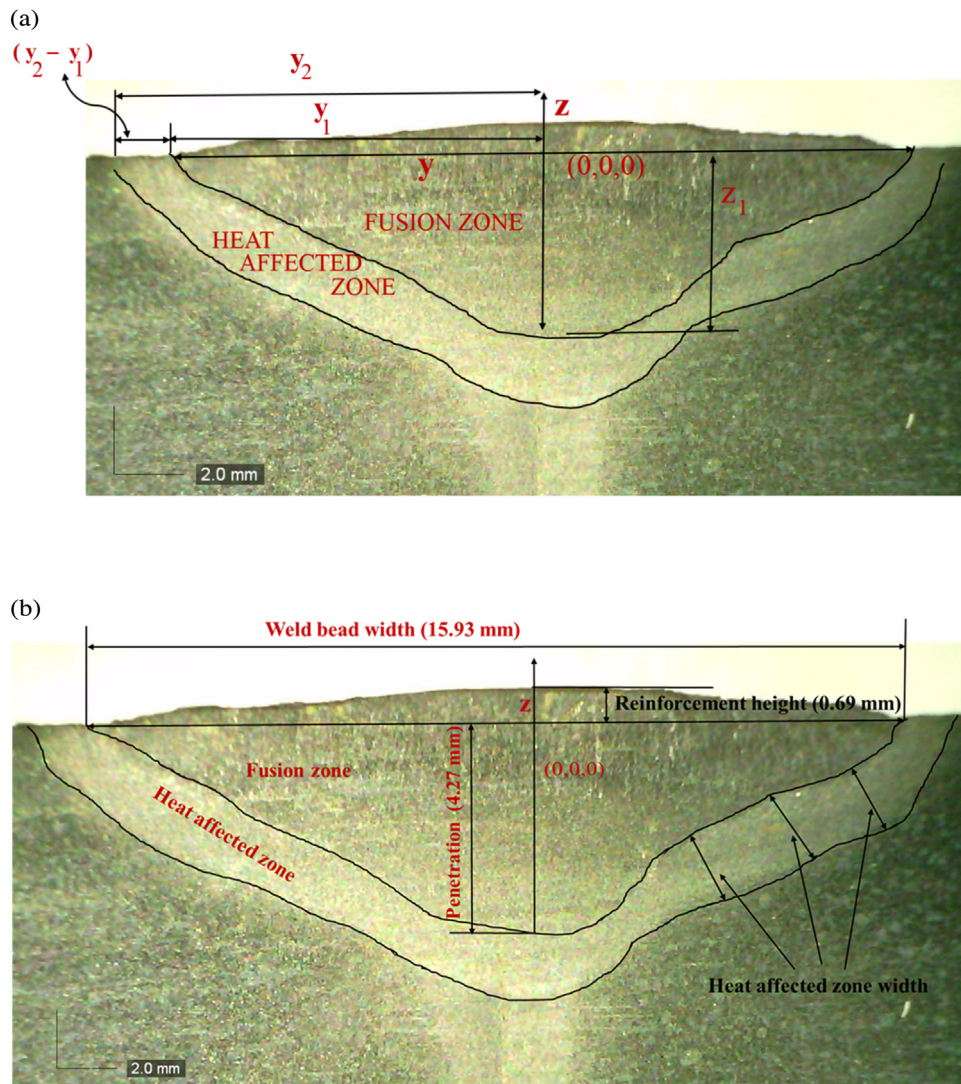


Fig. 16. Weld bead geometry when tilt angle is 34° (a) representation of the axis system, penetration and HAZ width (b) measured value of bead width, penetration and reinforcement height.

The validated analytical predictions indicate that the analytical method developed can offer a good predictability for the transient temperatures near the weld pool as well as away from the welding line, and the HAZ width. The newly developed heat source model can also be applicable to other welding processes that involve tilted heat source.

Appendix I.

Eq. (7c) is initially divided into three parts for the sake of simplicity as described in Eq. (A1). Thereafter, every part is integrated using general integral formula as described in Eqs. (A3)–(A5).

$$Ax^2 + By^2 + Cz^2 + Dxz = A\left(x + \frac{D}{2A}\right)^2 + \left(C - \frac{D^2}{4A}\right)z^2 + By^2 \quad (\text{A1})$$

$$\int_{-\infty}^{\infty} \int_{-\infty}^{\infty} \int_{-\infty}^{\infty} e^{-(Ax^2+By^2+Cz^2+Dxz)} dx dy dz = \frac{\pi^{3/2}}{\sqrt{AB(C - \frac{D^2}{4A})}} \quad (\text{A2})$$

where

$$\int_{-\infty}^{\infty} e^{-A\left(x + \frac{D}{2A}z\right)^2} dx = \frac{\sqrt{\pi}}{\sqrt{A}} \quad (\text{A3})$$

$$\int_{-\infty}^{\infty} e^{-By^2} dy = \frac{\sqrt{\pi}}{\sqrt{B}} \quad (\text{A4})$$

$$\int_{-\infty}^{\infty} e^{-\left(C - \frac{D^2}{4A}\right)z^2} dz = \frac{\sqrt{\pi}}{\sqrt{(C - \frac{D^2}{4A})}} \quad (\text{A5})$$

Appendix II.

Initially, a part of Eq. (11) is simplified as described in Eqs. (A6)–(A9), and then integration is carried out for every part as described in Eqs. (A10)–(A12)

$$-A\left(x'' + \frac{D}{2A}z''\right) - \frac{(x - x'')^2}{4\alpha(t - t'')} = -j(x'' + i)^2 - i^2 j \quad (\text{A6})$$

where

$$i = \frac{Dz'' - \frac{x-vt''}{gA}}{1 + \frac{1}{(gA)^2}}; j = 1 + \frac{1}{(gA)^2}; g = 4\alpha(t-t'') \quad (\text{A7})$$

When heat source is moving with constant speed v from time $t'' = 0$ tot $t'' = t$, x will be replaced by $(x-vt'')$ and Eq. (A6) is written as

$$-A \left(x'' + \frac{D}{2A} z'' \right) - \frac{(x-vt''-x'')^2}{4\alpha(t-t'')} = -j(x''+i_t)^2 - i_t^2 j \quad (\text{A8})$$

$$\text{where } i_t = \frac{Dz'' - \frac{(x-vt''-t'')}{gA}}{1 + \frac{1}{(gA)^2}} \quad (\text{A9})$$

$$\text{Hence, } \int_{-\infty}^{\infty} e^{-j(x''+i)^2 - i^2 j} dx'' = \frac{\sqrt{\pi}}{\sqrt{j}} \times e^{-i^2 j} \quad (\text{A10})$$

$$\begin{aligned} \int_{-\infty}^{\infty} e^{-(i^2 j - \frac{(z-z')^2}{g} - (C - \frac{D}{4A}) z'^2)} dz'' &= \\ \int_{-\infty}^{\infty} e^{(-[m(z'' - \frac{n}{m}) + (o - \frac{n^2}{m})])} dz'' &= \frac{\sqrt{n}}{\sqrt{m}} \times e^{-(o - \frac{n^2}{m})} \end{aligned} \quad (\text{A11})$$

where

$$i^2 j + \frac{(z-z')^2}{g} + \left(C - \frac{D^2}{4A} \right) z'^2 = m \left(z'' - \frac{n}{m} \right) + \left(o - \frac{n^2}{m} \right) \quad (\text{A12})$$

where

$$m = \frac{(AD)^2}{j} + C - \frac{D^2}{4A} - \frac{1}{g}, \quad n = \frac{z}{g} - \frac{DAx}{gj}, \quad o = \frac{(Ax)^2}{jg^2 A^2} - \frac{z^2}{g}; \quad (\text{A13})$$

$$\Delta T_2 = \int_0^t \left(\int_0^{\frac{\Delta l}{2}} \left(\int_{-\frac{E}{2}}^{\frac{E}{2}} \left(\int_{-P}^R \frac{(\Delta q_{ms} + \Delta q_{hf} + \Delta q_{ml})}{\rho c_p [(4\pi\alpha(t-t'')]^{3/2}] \times e^{-[\frac{(x-x'')^2}{4\pi\alpha(t-t'')}]} \times e^{-[\frac{(y-y'')^2}{4\pi\alpha(t-t'')}]} \times e^{-[\frac{(z-z'')^2}{4\pi\alpha(t-t'')}]} dz'' \right) dy'' \right) dx'' \right) dt'' \quad (\text{A23})$$

$$By''^2 + \frac{(y-y'')^2}{g} = p(y''-u)^2 + w \quad (\text{A14})$$

where

$$p = B + \frac{1}{g}; \quad u = \frac{\left(\frac{y}{g}\right)^2}{\left(B + \frac{1}{g}\right)}; \quad w = \frac{y^2}{g} - \frac{\left(\frac{y}{g}\right)^2}{\left(B + \frac{1}{g}\right)}; \quad (\text{A15})$$

$$\text{Hence, } \int_{-\infty}^{\infty} e^{-\left(By''^2 - \frac{(y-y'')^2}{g}\right)} dy'' = \frac{\sqrt{\pi}}{\sqrt{p}} e^{-w} \quad (\text{A16})$$

Therefore,

$$\begin{aligned} \int_{-\infty}^{\infty} \int_{-\infty}^{\infty} \int_{-\infty}^{\infty} \frac{q(x'', y'', z'') dx'' dy'' dz'' dt''}{\rho c_p [(4\pi\alpha(t-t'')]^{3/2}] \times e^{-[\frac{(x-x'')^2 + (y-y'')^2 + (z-z'')^2}{4\pi\alpha(t-t'')}]} \\ = \int_0^t \frac{\sqrt{\pi}}{\sqrt{j}} \times e^{-i^2 t^2 j} \times \frac{\sqrt{\pi}}{\sqrt{m}} \times e^{-(o_t - \frac{n_t^2}{m})} \frac{\sqrt{\pi}}{\sqrt{p}} e^{-w} dt'' \end{aligned} \quad (\text{A17})$$

$$\text{where } n_t = \frac{z}{g} - \frac{DA(x-t'')}{gj}; \text{ and } o_t = \frac{A(x-t'')^2}{jg^2 A^2} - \frac{z^2}{g}$$

Suppose $4\alpha(t-t'') = s$, then following equations can be written

$$\int e^{-\left(\frac{(x-x'')^2}{4\alpha(t-t'')}\right)} dx'' = \sqrt{\pi} \operatorname{erf} \left(\frac{x'' - x}{\sqrt{s}} \right) \quad (\text{A18})$$

$$\int e^{-\left(\frac{(y-y'')^2}{4\alpha(t-t'')}\right)} dy'' = \sqrt{\pi} \operatorname{erf} \left(\frac{y'' - y}{\sqrt{s}} \right) \quad (\text{A19})$$

$$\int e^{-\left(\frac{(z-z'')^2}{4\alpha(t-t'')}\right)} dz'' = \sqrt{\pi} \operatorname{erf} \left(\frac{z'' - z}{\sqrt{s}} \right) \quad (\text{A20})$$

Appendix III.

Eq. (16) is derived with the help of Eqs. (A23)–(A25) as described below.

$$\begin{aligned} dT_2 = & \frac{q_m dx'' dy'' dz''}{\rho c_p [4\pi\alpha(t-t'')]^{3/2}} \times e^{-\left[\frac{(x-x'')^2}{4\pi\alpha(t-t'')}\right]} \\ & \times e^{-\left[\frac{(y-y'')^2}{4\pi\alpha(t-t'')}\right]} \times e^{-\left[\frac{(z-z'')^2}{4\pi\alpha(t-t'')}\right]} \end{aligned} \quad (\text{A21})$$

$$\begin{aligned} dT_2 = & \frac{(\Delta q_{ms} + \Delta q_{hf} + \Delta q_{ml}) dx'' dy'' dz''}{\rho c_p [4\pi\alpha(t-t'')]^{3/2}} \times e^{-\left[\frac{(x-x'')^2}{4\pi\alpha(t-t'')}\right]} \\ & \times e^{-\left[\frac{(y-y'')^2}{4\pi\alpha(t-t'')}\right]} \times e^{-\left[\frac{(z-z'')^2}{4\pi\alpha(t-t'')}\right]} \end{aligned} \quad (\text{A22})$$

Therefore, the temperature increase due to heat transfer from molten electrode for time t along x direction is expressed as

The electrode and the welded plate are of same material.

Appendix IV.

HAZ is the weakest zone caused by the heating and cooling cycle of the welded zone. It is the part of the welded plate where metal is not melted but distinct microstructural change has taken place. This zone exists between the portions from the end of FZ to the lower critical zone of welded plate. Therefore, for mild steel, HAZ width is the distance between the portion where maximum temperature is 1684 K (melting temperature) to the portion where maximum temperature is 1000 K (lower critical temperature) (Klimpel et al., 2006).

With the help of Eqs. (2), (11), (15) and (19), and putting $x = vt''$, $y = 0$, $t = 144$ s, (as the length of the plate is 30 cm and travel speed is 7.5 m s⁻¹), $T(x-z, t) = T_1$ (melting temperature) = 1684 K, $T(x-z, t) = T_2$ (lower critical temperature) = 1000 K, T_0 (ambient temperature) = 313 K in Eq. (6), values of y , i.e., y_1, y_2 can be obtained where

$$\begin{aligned} y &= y_1 = \text{half of bead width, and } y_2 - y_1 \\ &= \text{HAZ width (as shown in Fig. 16(a))} \end{aligned} \quad (\text{A24})$$

It may be noted that $y=y_1$ when $T(x-z, t)=T_1$ and $y=y_2$ when $T(x-z, t)=T_2$ as tabulated in Table 3.

In a similar way, with the help of Eqs. (2), (11), (16) and (19d), and putting $x=vt''$, $z=0$ and $t=144\text{ s}$, (as length of the plate is 30 cm and travel speed is 12.5 cm/min), $T(x, y, z, t)=T_1$ (melting temperature) = 1684 K, T_0 (ambient temperature) = 313 K in Eq. (6), value of $z(z=z_1)$ can be obtained.

$$z_1 = \text{Penetration}(\text{asshowninFig.16(a)}) \quad (\text{A25})$$

References

- Bonifaz, E.A., Richards, N.L., 2009. Modeling cast IN-738 super alloy gas tungsten arc welds. *Acta Mater.* 57 (6), 1785–1794.
- Boumerzoug, Z., Derfouf, C., Baudin, T., 2010. Effect of welding on microstructure and mechanical properties of an industrial low carbon steel. *Engineering* 2, 502–506.
- Chandell, R.S., Hang, I., 1996. Effect of electrode geometry and tilt angle on the plate melting efficiency of the GAT welding process. *J. Mater. Sci. Lett.* 15, 2099–2100.
- Eager, T.W., Tsai, N.S., 1983. Temperature fields produced by traveling distributed heat sources. *Weld. J.* 62 (12), 346s–355s.
- Ghosh, A., Chattopadhyay, H., 2013. Mathematical modeling of moving heat source shape for submerged arc welding process. *Int. J. Adv. Manuf. Technol.* 69 (9–12), 2691–2701.
- Ghosh, A., Barman, N., Chattopadhyay, H., Bag, S., 2013. Modelling of heat transfer in submerged arc welding process. *Proc. Inst. Mech. Eng. B* 227, 1467–1473.
- Goldak, J.A., Akhlaghi, M., 2006. Computational Welding Mechanics. Springer Science & Business Media, pp. 46.
- Goldak, J., Chakravarti, A., Bibby, M.A., 1984. A new finite element model for welding heat sources. *Mettal. Trans. B* 1, 299–305.
- Goyal, V.K., Ghosh, P.K., Saini, J.S., 2009. Analytical studies on thermal behaviour and geometry of weld pool in pulsed current gas metal arc welding. *J. Mater. Process. Technol.* 209 (3), 1318–1336.
- Grujicic, M., Arakere, G., Pandurangan, B., Ochterbeck, J.M., Yen, C.F., Cheeseman, B.A., Reynolds, A.P., Sutton, M.A., 2012. Computational analysis of material flow during friction stir welding of AA5059 aluminum alloys. *J. Mater. Eng. Perform.* 21, 1824–1840.
- Klimpel, A., Balcer, M., Klimpel, A.S., Rzeznikiewicz, A., 2006. The effect of the method and parameters in the GMA surfacing with solid wires on the quality of puddling welds and the content of the material in the overlay. *Weld. Int.* 20, 845–850.
- Kumar, A., Debroy, T., 2007. Heat Transfer and fluid flow during Gas Metal Arc Fillet Welding for various joint configurations and welding positions. *Mettal. Mater. Trans.* 38A, 506–519.
- Mahapatra, M.M., Datta, G.L., Pradhan, B., Mandal, N.R., 2006. Three dimensional finite element analyses to predict the effects of SAW process parameters on temperature distribution and angular distortions and in single pass butt joints with top and bottom reinforcements. *Int. J. Press. Vessel Pip.* 83, 721–729.
- Mishra, S., Lienert, T.J., Johnson, M.Q., DebRoy, T., 2008. An experimental and theoretical study of gas tungsten arc welding of stainless steel plates with different sulfur concentrations. *Acta Mater.* 56 (9), 2133–2146.
- Moghaddam, M.A., Golmazerji, R., Kolahan, F., 2016. Multi-variable measurements and optimization of GMAW parameters for API-X42 steel alloy using a hybrid BPNN-PSO approach. *Measurement* 92, 279–287.
- Nguyen, N.T., Ohta, A., Matsuoka, K., Suzuki, N., Maeda, Y., 1999. Analytical solutions for transient temperature of semi-infinite body subjected to 3D moving heat sources. *Weld. J. N. Y.* 78, 265s.
- Nilsson, H., Choquet, I., Sass-Tisovskaya, M., 2011. 8th International Conference on Heat Transfer, Fluid Mechanics and Thermodynamics, implementation of a 3D solver for electric arc welding, coupling fluid mechanics with electromagnetics. In: International Conference on Heat Transfer, Fluid Mechanics and Thermodynamics, 11–13 July, Pointe Aux Piments, Mauritius.
- Parkitny, R., Winczek, J., 2013. Analytical solution of temporary temperature field in half-infinite body caused by moving tilted volumetric heat source. *Int. J. Heat Mass Transfer* 60, 469–479.
- Parvez, S.M., Nash, D.H., Fawad, H., Galloway, A., 2013. Effect of torch angle on arc properties and weld pool shape in stationary GTAW. *J. Eng. Mech.* 139, 1268–1277.
- Rosenthal, D., 1946. The theory of moving source of heat and its application to metal transfer. *Transitions ASME* 43 (11), 849–866.
- Winczek, J., 2008. Modelling of HAZ in rectangular prismatic steel casts regenerated by weave bead up. *Arch. Foundry Eng.* 8 (1), 331–336, Special Issue.
- Winczek, J., 2010. Analytical solution to transient temperature field in a half-infinite body caused by moving volumetric heat source. *Int. J. Heat Mass Transfer* 53, 5774–5781.
- Winczek, J., 2011. New approach to modeling of temperature field in surfaced steel elements. *Int. J. Heat Mass Transfer* 54, 4702–4709.
- Winczek, J., 2012. A simplified method of predicting stresses in surfaced steel rods. *J. Mater. Process. Technol.* 212, 1080–1088.